Laminar Separation Bubble Noise on a Propeller Operating at Low Reynolds Numbers

Grande, E.; Ragni, D.; Avallone, F.; Casalino, D.

DOI
10.2514/1.J061691

Publication date
2022

Document Version
Final published version

Published in
AIAA Journal: devoted to aerospace research and development

AIAA JOURNAL
Vol. 60, No. 9, September 2022

Laminar Separation Bubble Noise on a Propeller Operating at Low Reynolds Numbers

Edoardo Grande,* Daniele Ragni,† Francesco Avallone,‡ and Damiano Casalino§
Delft University of Technology, 2629 HS Delft, The Netherlands

https://doi.org/10.2514/1.J061691

This paper explains the presence and relevance of noise caused by a laminar separation bubble (LSB) on a propeller operating at a low Reynolds number. Microphone measurements of a propeller with both clean and forced boundary-layer transition blades are carried out in an anechoic wind tunnel by varying the propeller advance ratio J from 0 to 0.6, corresponding to a tip Reynolds number ranging from $4.3 \cdot 10^4$ to 10^5. The flow behavior on the blade surface and around the propeller is investigated with oil-flow visualizations and particle image velocimetry. At $J = 0.4$ and 0.6, vortex shedding from the LSB causes high-frequency noise that appears as a hump in the far-field noise spectra. Forcing the location of the boundary-layer transition suppresses the LSB and, consequently, the hump, reducing the noise emission of about 5 and 10 dB at $J = 0.4$ and 0.6, respectively. The fact that the hump is caused by LSB vortex shedding noise is further assessed by using a semi-empirical noise model; it shows that the hump is constituted by tones of different amplitudes and frequencies, emitted at different spanwise sections along the blade.

Nomenclature

c	=	blade chord, m
D	=	propeller diameter, m
f	=	frequency, Hz
J	=	advance ratio
R	=	propeller radius, m
Re_c	=	chord-based Reynolds number
V_∞	=	freestream velocity, m/s
α	=	angle of attack, deg
ψ	=	propeller azimuthal angle, deg

Subscript

∞	=	freestream condition

I. Introduction

LOW-REYNOLDS-NUMBER flows over rotating blades is of great interest for the design of several devices, such as unmanned aerial vehicles, micro aerial vehicles, and urban wind turbines. These devices employ small-scale rotors, which operate at a chord-based Reynolds number Re_c ranging from 10^4 to 10^5. At such low Reynolds numbers, the boundary layer on the propeller blades is usually subjected to a laminar separation, even at low angles of attack. The separated shear layer gains momentum from the freestream and reattaches as turbulent boundary layer, forming a laminar separation bubble (LSB) [1]. The LSB influences the aerodynamic performances and can be responsible of noise radiation.

The works from Grande et al. [2] and Leslie et al. [3] focus on the different noise sources that are simultaneously present in a small-scale propeller. In particular, they showed that, for some operating conditions, the vortex shedding generated from an LSB constitutes the predominant noise source at high frequency and that it is responsible for a hump in the far-field noise spectra. However, the research on these kinds of propellers is limited by several numerical and experimental challenges. On the numerical side, the main challenges are related to the capability of the computational fluid dynamics (CFD) solver to correctly predict the transitional flow behavior [4]. On the experimental side, flow velocimetry suffers from the small chordwise dimensions of the blades and to fact that the system is rotating. Furthermore, acoustic measurements are contaminated by electrical motor noise [5,6] and vibrations of the test rig. The studies focusing on steady airfoils reveal that, as the angle of attack (or Reynolds number) increases, the LSB moves upstream and decreases in length [7]. The decrease in length of the LSB as the angle of attack increases continues until the separation and reattachment point occur at the same point (in the vicinity of the leading edge) and the bubble bursts. In this case a laminar separation is still present, but the separated shear layer is not able to reattach anymore. This causes a pronounced decrease in lift and increase in drag. At very low Reynolds numbers, an LSB can burst at low angles of attack and the lift polar shows a substantial decrease of the curve slope due to a lower suction peak (with respect to the corresponding inviscid case), as shown by Yarusevych et al. [8] and by Marchman and Abtahi [9]. The sketch in Fig. 1 (left) illustrates the general trends of the reattachment point versus the angle of attack, at different Reynolds numbers ($Re_1 < Re_2 < Re_3$). The angle of attack at which the LSB starts forming (indicated by the horizontal dashed lines) depends on the Reynolds number. In particular, when Re increases, the LSB starts forming at a lower angle of attack [10]. The corresponding lift coefficient c_l curve is shown in Fig. 1 (right). The visible lower c_l slope for the red curve, corresponding to the lowest Reynolds number Re_1, is related to the bubble bursting at low α or, in other words, to a flow separation with no reattachment.

An LSB located sufficiently close to the airfoil trailing edge is responsible of tonal noise emission [11]. Indeed, coherent vortices, a result of amplified instability (Tollmien–Schlichting) waves into the laminar boundary layer, roll up over the separated shear layer and produce tonal noise during their passage over the trailing edge. The coherence of the vortical structures at the trailing edge is a necessary condition for tonal noise emission. The acoustic pressure waves scattered at the trailing edge propagate upstream and trigger the generation of new instability waves, in turn leading to vortex shedding. Hence, a so-called "feedback loop" is created between the trailing edge and the upstream point where the hydrodynamic instabilities are formed. It is not clear yet whether the presence of a feedback loop is a necessary condition for the tonal noise generation, and there is no agreement on the physics and exact chordwise extent of the feedback loop [12].

Arbey and Bataille [13] found that, in the presence of vortex shedding from LSB, the spectrum of the radiated noise, for a class of NACA airfoils, consists of a broadband hump (centered at a

Received 31 January 2022; revision received 8 May 2022; accepted for publication 11 May 2022; published online 21 June 2022.

*Ph.D. Candidate, Aerodynamics, Wind Energy, Flight Performance and Propulsion Department; e.grande@tudelft.nl. Member AIAA.
†Associate Professor, Aerodynamics, Wind Energy, Flight Performance and Propulsion Department; d.ragni@tudelft.nl. Member AIAA.
‡Assistant Professor, Aerodynamics, Wind Energy, Flight Performance and Propulsion Department; f.avallone@tudelft.nl. Member AIAA.
§Professor, Aerodynamics, Wind Energy, Flight Performance and Propulsion Department; d.casalino@tudelft.nl. Member AIAA.

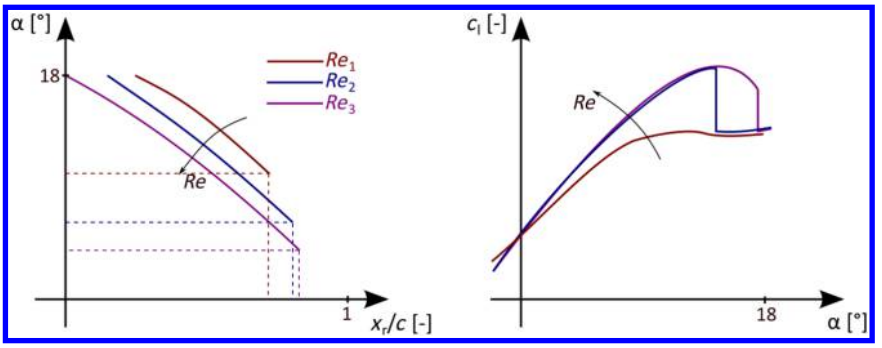

Fig. 1 Sketch of the chordwise locations of the reattachment point (left) and lift coefficient curves at different Reynolds numbers (right).

frequency f_s) and a dominant (or central) tone (at a frequency $f_{n_{MAX}}$) surrounded by a series of regularly spaced tones at frequencies f_n. Paterson et al. [14] observed that the main tone frequency exhibits the so-called "ladder structure"; i.e., for a small range of freestream velocities U_∞, it increases as $U_\infty^{0.8}$ and, at certain velocities, it jumps to higher frequencies following a new $U_\infty^{0.8}$ power relationship with the velocity. The average trend of the main tone frequency (obtained by fitting a straight line through all the data points) follows a 3/2 power of the freestream velocity; hence $f_{n_{MAX}} \propto U_\infty^{1.5}$. On the contrary, the tone frequency pattern from the investigation of Nash et al. [15] does not exhibit any ladder-like structure. Pröbsting et al. [16] found that the acoustic spectrum is characterized by a primary tone over a large range of Reynolds numbers and angles of attack and that it is subject to at least one ladder-type transition for a specific Re_c. Moreover, they proved that the tonal noise emission is dominated by suction side vortex shedding at low Reynolds numbers and pressure side vortex shedding at higher Reynolds numbers. While Paterson's model estimates only the vortex shedding tone frequency, the only available model that predicts the amplitude of the tones is the airfoil self-noise model from Brooks et al. [17] (in the following referred as BPM model). The latter is a semi-empirical model based on a wind tunnel data set on NACA 0012 airfoils of different chord length. It is unknown if the current knowledge about noise generation due to laminar vortex shedding from steady airfoils applies also to rotating blades. In this case, the spanwise variation of velocity and angle of attack can influence the formation of the LSB and the coherence of the shed vortices.

The aim of the paper is to study the characteristics of the LSB for a propeller operating at low Reynolds numbers and to show how the LSB contributes to a significant noise emission. To this purpose, a small-scale propeller is tested at a tip Reynolds number between $4.3 \cdot 10^4$ and 10^5. Far-field noise measurements, phase-locked stereoscopic particle image velocimetry (PIV), and oil-flow visualization are used to quantify the noise radiation and to visualize the flow around the propeller and on the blade surface, respectively. A comparison is presented for the case of the propeller with smooth surface and with a turbulator applied on the blade surface to force the location of the transition of the boundary layer from laminar to turbulent. A physical interpretation of the acoustic spectra is given by extending the BPM model to rotating blades.

The paper is structured as follows. In Sec. II the propeller geometry is presented together with the experimental setup. Section III illustrates the extension of the BPM model to rotating blades. Section IV shows the oil-flow and PIV results, while the experimental and numerical noise spectra are illustrated in Sec. V. Finally, the main conclusions of the work are summarized in Sec. VI.

II. Propeller Geometry and Experimental Setup

The propeller used for this research is inspired by an APC 9×6. It is a two-bladed propeller, constituted of NACA 4412 airfoil sections, with a diameter $D = 30$ cm. Measurements are conducted both with a smooth blades surface (denoted as clean) and with a turbulator applied on the suction side of the propeller blade (denoted as forced-BL s.s.), on the pressure side (denoted as forced-BL p.s.), and on both pressure and suction side (denoted as forced-BL). The turbulator fixes the boundary-layer transition location, and it is realized as a flat strip with a thickness of 0.08 mm and a chordwise length of 1 mm, and it is applied at 25% of the chord. The propeller is tested in the anechoic tunnel (A-tunnel) of TU Delft. The A-tunnel is a vertical, open-jet wind tunnel, and the exit nozzle employed is circular, with an exit diameter of 0.60 m and a contraction ratio of 15:1. A more detailed description of the propeller geometry and test rig can be found in Ref. [2], whereas the A-tunnel details of the flow and acoustics characterization can be found in Ref. [18].

For the acoustic measurements, the propeller is operated at three rotational velocities, 4000, 5000, and 6000 revolutions per minute (rpm), over a range of advance ratios $J = V_\infty/nD$ between 0 and 0.6 (where V_∞ is the axial flow speed in meter/second, n is the propeller rotational frequency in hertz, and D is the propeller diameter in meter). The tip Reynolds number is varied from $4.3 \cdot 10^4$ to 10^5. The operating conditions are summarized in Table 1. The flow measurements are conducted over a reduced test matrix, i.e., 4000 rpm and all the J reported in Table 1.

A. Acoustic Measurements

The acoustic measurements are performed by means of an arc of microphones, constituted by 7 G.R.A.S. 46BE 1/4″ free-field microphones, having a frequency range between 4 Hz and 80 kHz and a maximum SPL of 160 dB. As shown in Fig. 2, the microphone arc has a radius of $4D$ (1.2 m) and the angle between each microphone is 10°. The microphones are calibrated using a G.R.A.S. 42AA pistonphone with a calibration level of 114 dB re. 20 μPa. The uncertainty of the calibration is less than 0.09 dB (99% confidence level). The data acquisition system consists of a National Instrument PXIe-4499 sound and vibrations data acquisition module. Microphone voltages have been recorded for a duration of 30 s at a frequency rate of 100 KHz. Fourier transformed data are obtained with 750 Welch blocks, 50% overlap and Hanning windowing, corresponding to a bandwidth of 25 Hz.

B. PIV Measurements

Stereoscopic PIV measurements are conducted to study the flow around the cross section of the blade at $r/R = 0.6$ and in the propeller wake. The flow is seeded with particles lower than 1 μm median diameter produced by a SAFEX Twin Fog generator with SAFEX-Inside-Nebelfluid, a mixture of diethylene glycol and water. Illumination is provided by a double-cavity Quantel Evergreen EVG00200 Nd:YAG laser with 200 mJ/pulse energy. Figure 3 shows the laser and camera configuration adopted for both types of measurements. A total of four Imager sCMOS cameras (2560×2160 px), two for the suction side and two for the pressure side, equipped with Scheimpflug adapters

Table 1 Propeller operating conditions

J	rpm	V_∞, m/s	rpm	V_∞, m/s	rpm	V_∞, m/s
0.0	4000	0.0	5000	0	6000	0
0.24	4000	4.8	5000	6	6000	7.2
0.4	4000	8.0	5000	10	6000	12
0.6	4000	12	5000	15	6000	18

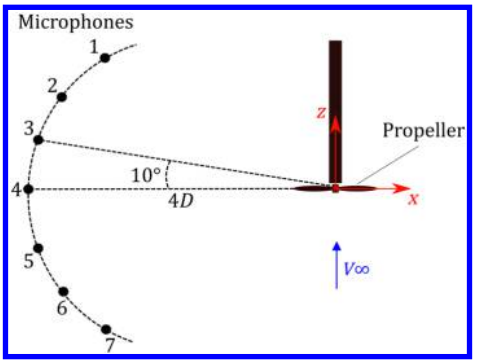

Fig. 2 Microphone array configuration.

Table 2 Details of PIV setup for the cross-sectional and wake measurements

Imaging parameter	Wake measurement	Cross-sectional measurement
Camera	2 Imager sCMOS	4 Imager sCMOS
Number of pixels, px	2560×2160	2560×2160
Pixel size, μm	6.5×6.5	6.5×6.5
Focal length, mm	60	200
Magnification	0.1	0.37
Imaging resolution, px/mm	≈15	≈56
FOV, cm^2	16×16	4.5×4
Spatial resolution, mm	≈0.28	≈0.4
f#	8	11

and four Nikon lenses with 200 mm focal length at f# 11 are used for the cross-sectional measurements, whereas two imager sCMOS cameras equipped with Scheimpflug adapters and two Nikon lenses with 60 mm focal length at f# 8 are used for the wake measurements. The camera calibration, acquisition, and postprocessing are carried out with the LaVision Davis 8.4 software.

To visualize the entire flowfield around the blade cross section, a beam splitter is used to create two laser sheets of about 1 mm of thickness, one illuminating the suction side of the cross section and one the pressure side (see Fig. 3a). Hence, the final field of view is the combination of two fields of view. To converge statistics, sets of 500 images are recorded in phase-locked mode; thus a trigger signal from the encoder mounted on the motor shaft is used to synchronize laser and camera. For the cross-sectional measurements, the images are acquired when the propeller section is aligned with the laser plane, as depicted in Fig. 3a (bottom). For the wake measurements instead, three propeller azimuthal angles are chosen, i.e., $\Psi = 0°$, $\Psi = 45°$, and $\Psi = 90°$ (see Fig 3b).

The images are processed with a cross-correlation algorithm employing the window deformation iterative multigrid [19] with final interrogation window size of 24×24 pixels and 75% overlap for the sectional measurements and 16×16 pixels and 75% overlap for the wake measurements. Spurious vectors are identified through a median filter and replaced by interpolation. The main parameters of the current PIV setup are reported in Table 2.

A self-calibration through a disparity correction procedure is used [20], in order to refine the target calibration by correlation of the particle images between the two cameras. The residual average misalignment is equal to 0.03 px for the cross-sectional measurements and 0.005 px for the wake measurements. The phase-locked PIV measurements of this study are mainly affected by random errors, as the cross-correlation uncertainty. The effect of this error scales with $1/\sqrt{N}$ (where N is the number of images), due to statistical convergence. The cross-correlation uncertainty is in a range of 0.05–0.1 px [21], for a multipass algorithm ending with a windows size between 24×24 px and 16×16 px. The corresponding error based on the value of maximum instantaneous velocity, encountered at the airfoil suction side, is of the order of 0.9%, whereas for the minimum velocity, encountered at the airfoil leading edge, it is equal to 5%. Therefore, the overall uncertainties on the maximum and minimum mean velocities are assessed at 0.04 and 0.22%. On the other hand, the overall uncertainty relative to the maximum and minimum velocity fluctuations is of the order of 1.7 and 14%, respectively.

C. Oil-Flow Visualizations

To visualize the surface flow pattern on the propeller blade, surface oil-flow visualizations are carried out. A fluorescent mixture obtained from 50 mL of Shell Ondina Oil 15 liquid-paraffin wax

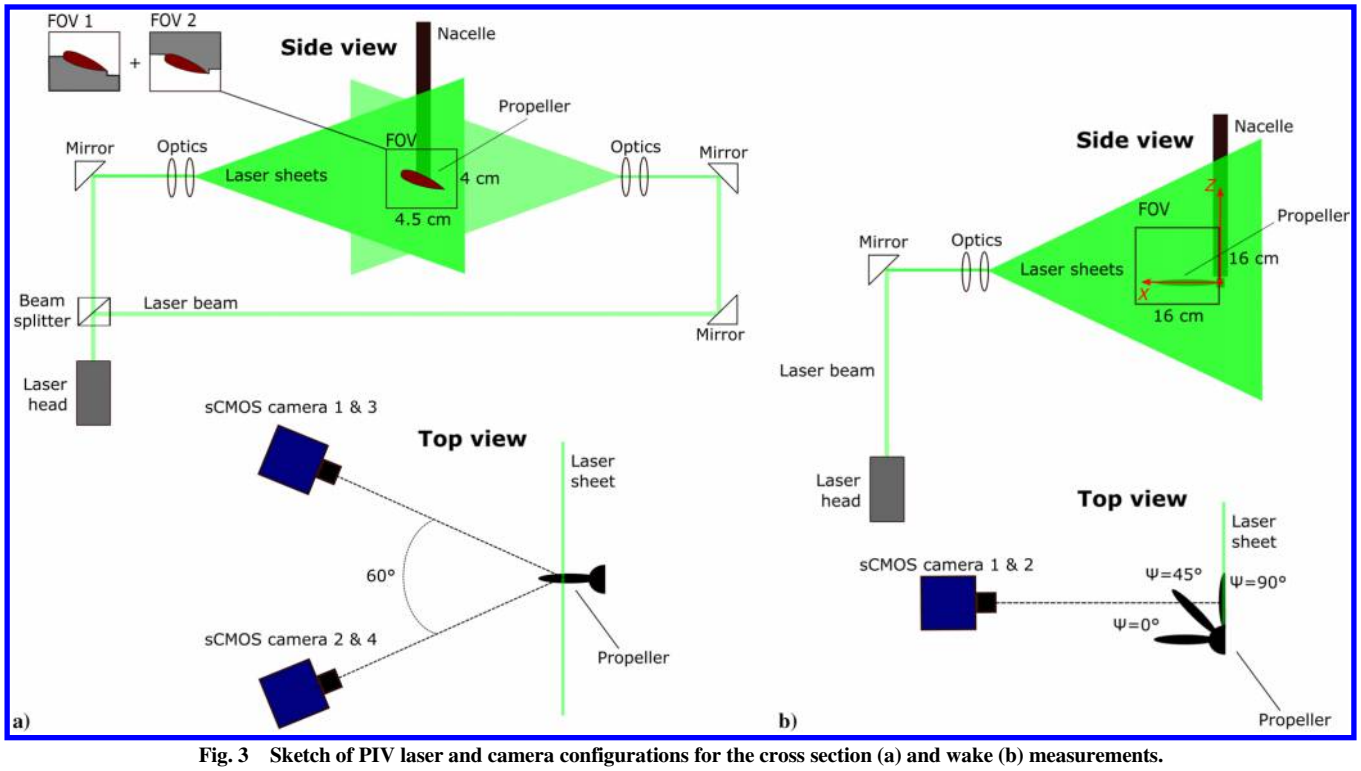

Fig. 3 Sketch of PIV laser and camera configurations for the cross section (a) and wake (b) measurements.

and 15–25 drops of fluorescent oil additive A-680 is used. The oil-flow tests are conducted as follows. A film of oil is applied on the blade surface. The propeller is brought to the required operating conditions and is run for about 8–10 minutes to let the mixture to properly establish on the blade surface. Finally, the propeller is slowly stopped, and then it is illuminated at rest with an ultraviolet lamp with a wide aperture and pictures of the blade surface are taken.

III. Extension of the BPM Model to Rotating Blades

This section illustrates how the BPM model [17], originally developed to predict self-generated noise of a steady airfoil encountering smooth flow, is extended to a rotating blade. To this purpose, a strip approach is applied; i.e., the propeller blade is divided into N spanwise elements (sources) and, for each of them, the noise contribution is computed by using the BPM model. The main assumption of the strip theory is that there is no aerodynamic interaction between the elements; thus the effect of the spanwise velocity component is discarded. The airfoil self-noise mechanisms implemented in the current work are the laminar boundary-layer vortex shedding (LBL-VS) noise and turbulent boundary-layer trailing edge noise (TBL-TE). Following the BPM approach, the LBL-VS noise spectrum in 1/3-octave for the ith strip can be written as

$$\mathrm{SPL}^{i}_{\mathrm{LBL-VS}}(X,Y,Z) = 10\log\left(\frac{L_i\delta_p M^5 \bar{D}_h}{r_e^2}\right) + G_1\left(\frac{St'}{St_{\mathrm{peak}}{}'}\right) + G_2\left[\frac{Re_c}{(Re_c)_0}\right] + G_3(\alpha) \tag{1}$$

where the superscript i refers to the ith strip, L_i is the spanwise length of the strip, δ_p is the boundary-layer thickness at the trailing edge of the blade for the pressure side, M is the freestream Mach number, r_e is the absolute source–observer distance, $\bar{D}_h$ is the directivity function for the high-frequency limit, St' is the Strouhal number defined as $St' = f\delta_p/U_\infty$ (with f being the frequency vector and U_∞ the freestream velocity), Re_c is the chord-based Reynolds numbers, and α is the angle of attack. For details about $\bar{D}_h$, $St_{\mathrm{peak}}{}'$, $(Re_c)_0$, G_1, G_2, and G_3, the reader can refer to Brooks et al. [17]. The TBL-TE noise spectrum in 1/3-octave for the ith strip is instead modeled as follows:

$$\mathrm{SPL}^{i}_{\mathrm{TBL-TE}}(X,Y,Z) = 10\log(10^{(\mathrm{SPL}_p/10)} + 10^{(\mathrm{SPL}_s/10)} + 10^{(\mathrm{SPL}_\alpha/10)}) \tag{2}$$

where the three terms in the equation account for the attached TBL at the pressure side (SPL_p), for the attached TBL at the suction side (SPL_s), and for the separated boundary layer at high angles of attack (SPL_α). The full expressions for these three terms can be found in Ref. [17].

The quantities δ_p and α constitute the main input parameters of the LSB-VS noise model, while δ_p^*, δ_s^* (boundary-layer displacement thickness at the pressure and suction side), and α constitute the main input parameters for the TBL-TE noise model. These parameters are predicted by using Opty∂B − BEMT, which is a tool for the prediction of the propeller loads, based on blade element momentum theory formulation with uniform inflow. Details about the tool can be found in the work of Casalino et al. [22], where the tool has been validated against experimental and numerical results.

When calculating the SPL contribution of the ith strip from Eq. (1), a local reference frame (x, y, z) shown in Fig. 4 (right) and located at the midspan of the strip is used. The axes x, y, z are the chordwise, spanwise, and wall-normal components, respectively. On the other hand, the position of the observer is given in the rotor fixed reference system (X, Y, Z), shown in Fig. 4 (left), where the$X$ and Y axes are in the rotor plane and the Z axis is parallel to the freestream. Therefore, a coordinate transformation is applied to express the position of the observer, given in (X, Y, Z), with respect to (x, y, z). To account for the Doppler effect, a frequency shift [23] is applied to each strip as

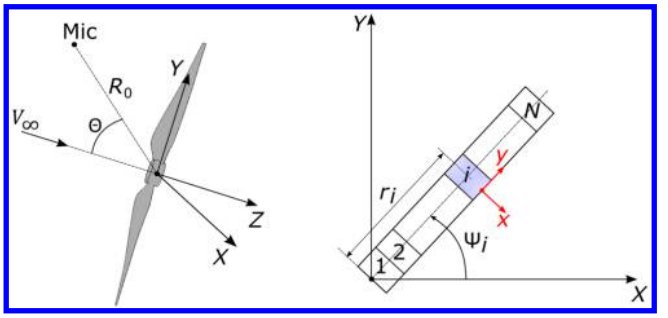

Fig. 4 Representation of the rotor fixed reference frame (left) and the propeller strip reference frame (right).

$$\frac{\omega_e}{\omega_o} = 1 + M_b \sin\Psi \sin\Theta \tag{3}$$

In the latter, ω_e is the emitted frequency from the source, ω_o is the frequency at the observer location, M_b is the source Mach number, Ψ is the source azimuthal position, and Θ is the observer angle (see Fig. 4). Finally, the total noise contribution is computed by assuming fully uncorrelated sources and averaging over all the azimuthal positions of the blade by means of

$$\mathrm{SPL}(x,y,z) = \frac{B}{2\pi}\int_0^{2\pi}\left(\frac{\omega_e}{\omega_o}\right)\mathrm{SPL}^{i}(x,y,z)\mathrm{d}\Psi \tag{4}$$

where B is the number of blades.

The vortex shedding noise frequency for each blade strip is also estimated by means of Paterson's power law relationship (mentioned in Sec. I). He postulated that the vortex shedding phenomenon from an airfoil qualitatively resembles the shedding associated to bluff bodies. Therefore a Strouhal number St of 0.2, defined as $St = 2f\delta_{\mathrm{TE}}/U_\infty$ (with δ_{TE} being the airfoil boundary-layer thickness at the trailing edge), has been taken as nondimensional frequency scaling law. Using for δ_{TE} the Blasius solution for a flat plate [24], it follows

$$f = K\frac{U_\infty^{1.5}}{\sqrt{c\nu}} \tag{5}$$

where $K = 0.02$, c is the airfoil chord, and ν is the kinematic viscosity of the fluid.

IV. Aerodynamic Characterization

A. Oil-Flow Visualizations

Figure 5 shows the oil-flow visualizations of the suction side of the propeller blade for both the clean and forced-BL cases at 4000 rpm and J varying from 0 to 0.6. Because the oil, especially at the tip region, is subjected to the propeller centrifugal force, the oil-flow results are only used to show the presence of an LSB, and not to retrieve the streamlines direction. The blade portion where the thickness oil accumulates (green area marked with S) represents regions with flow separation. These regions are characterized by a chordwise pressure gradient that is almost zero and the flow is predominantly radial due to the centrifugal force.

The clean case (Fig. 5, top) reveals a presence of an LSB at J between 0 and 0.4. The LSB is represented by the green region enclosed between the separation and reattachment lines, highlighted with dashed magenta and red lines, respectively. The LSB length increases with J because of a decrease of the local angle of attack along the blade. Unlike the other cases, at $J = 0$ the LSB does not extend up to the tip and this is ascribed to the tip vortex that washes out the LSB at the tip region [25,26]. For the case $J = 0.6$, the flow separates but it is not very clear if it reattaches in proximity of the trailing edge. Thus, a bubble bursting might occur.

When the turbulator is used (Fig. 5, bottom), the LSB is suppressed and all the cases exhibit a similar behavior. After the turbulator line the flow is attached and eventually separates close to the trailing edge. The separated region extends up to the tip only at $J = 0$ and reduces

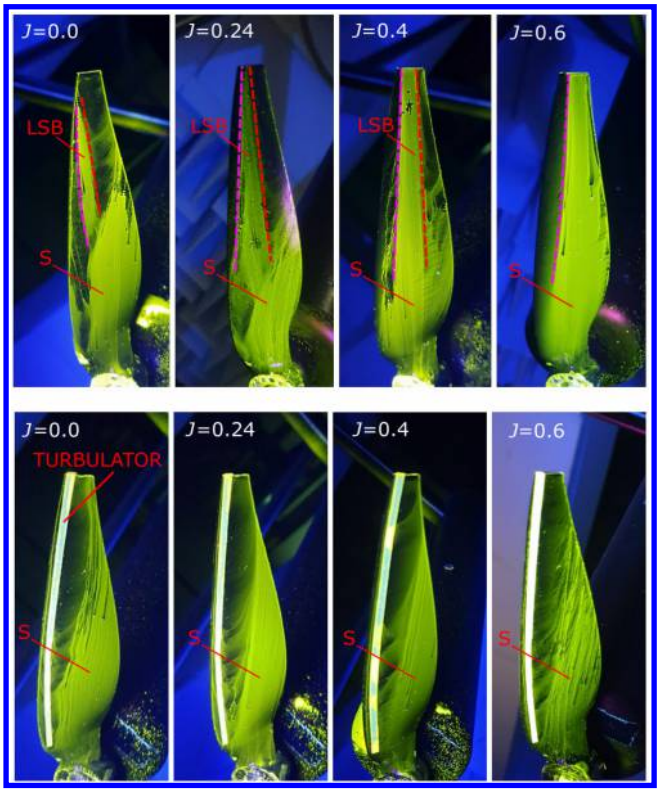

Fig. 5 Oil flow visualizations of the suction side of the clean blade (top) and of the forced-BL blade (bottom) at 4000 rpm and $J = 0$, 0.24, 0.4, and 0.6.

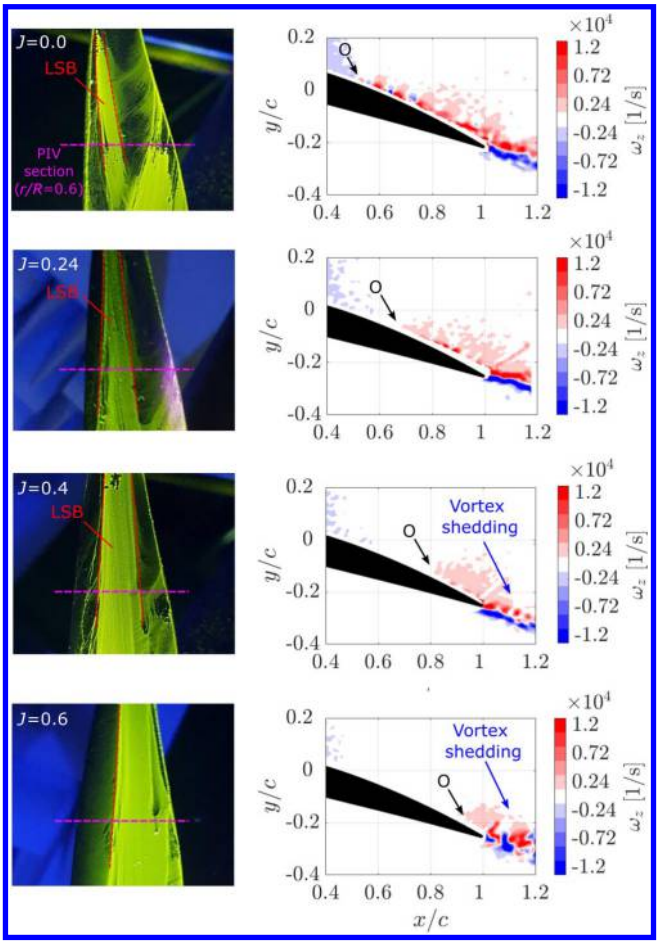

Fig. 6 Instantaneous spanwise vorticity distribution (right) around the clean blade cross section at $r/R = 0.6$ and oil-flow visualizations of the blade suction side at 4000 rpm. From top to bottom: $J = 0$, $J = 0.24$, $J = 0.4$, and $J = 0.6$.

in size as the advance ratio increases. This is probably due to the global decrease of the angle of attack over the entire blade as J increases.

B. Vorticity Field Around the Cross Section at $r/R = 0.6$

Figure 6 shows the instantaneous spanwise vorticity distribution (obtained with finite difference of order two from the PIV velocity fields) around the cross section of the clean blade at $r/R = 0.6$ at 4000 rpm and J varying from 0 to 0.6. The x and y axes are normalized with respect to the local airfoil chord and centered at the airfoil leading edge. Each vorticity field is adjacent to the corresponding oil-flow visualization of the blade suction side. The cross section at $r/R = 0.6$ is marked with the horizontal magenta line.

The cases at $J = 0.4$ and 0.6 exhibit coherent vortices in the near wake region ($1 < x/R < 1.2$), forming a vortex shedding. For the other two cases, i.e., $J = 0$ and 0.24, coherent structures in the near wake cannot be identified. Indeed, at low advance ratios the LSB has a smaller length and it is closer to the leading edge, as shown from the oil-flow patterns in the left side of the figure. As a consequence, the vortex shedding is characterized by structures with a lower coherence and length scale, which might be not captured from the current PIV setup. The surface point on the suction side where the vorticity is nonzero (marked with O) moves toward the trailing edge as J increases, in agreement with the downstream displacement of the LSB. It is relevant to note that the length scale of the structures at $J = 0.6$ is larger compared with the case at $J = 0.4$. This is related to the laminar separation without reattachment, as mentioned in the previous section. In fact, as shown by Yarusevych et al. [27], when the flow fails to reattach, the scale of the wake structures is noticeably larger.

The instantaneous vorticity fields at $J = 0.4$ and 0.6 are used to estimate the wake shedding frequency, adopting a statistical approach. To this purpose, the vorticity is extracted in the wake region and the two-dimensional spatial autocorrelation of the vorticity field is computed. Hence, for each frame, the characteristic wavelength λ of the vortices is calculated from the position of the autocorrelation peak and stored in an array. Lastly, the shedding frequency f_s is retrieved as $f_s = V_{\text{conv}}/\lambda$, where V_{conv} is the convection velocity, computed from the PIV velocity field. Figures 7a and 7b show the 2D autocorrelation coefficient $R_{xx}(\lambda)$ of a single vorticity field for the cases $J = 0.6$ and 0.4, respectively. As expected, they exhibit a unitary peak at $\lambda_x = \lambda_y = 0$ and a second peak with an amplitude of about 0.45 that is associated to the wavelength of the vortices. Spurious peaks with an amplitude lower than 0.2 are discarded. The arrays with the calculated wavelengths λ for each frame are fitted with Gaussian distributions (see Figs. 7c and 7d). The final wavelengths are chosen as the mean value of each distribution and they are equal to $\lambda = 2$ mm at $J = 0.4$ and $\lambda = 2.3$ mm at $J = 0.6$. The corresponding vortex shedding frequencies are 9635 and 8600 Hz for $J = 0.4$ and 0.6, respectively.

C. Vorticity Field in the Propeller Slipstream

To extend the above discussion to the entire blade, the Y component of the vorticity has been calculated in a plane in the propeller slipstream region for two cases: $J = 0$ (Fig. 8a) and $J = 0.4$ (Fig. 8b). The three columns in the figure represent three different propeller azimuthal angles: $\Psi = 0°$ (left), $\Psi = 45°$ (center), and $\Psi = 90°$ (right). The flow direction is from bottom to top, and the X and Y axes are centered at the rotor center (see Fig. 3b, top) and normalized with respect to the propeller radius. At $J = 0.4$ (Fig. 8b), the propeller presents a well-defined tip vortex together with a positive/negative vorticity region distributed along the entire blade, where different vortex cores are identified. This can be related to the footprint of the structures shed from the LSB, identified in Fig. 6, which are convected into the wake. These structures appear to be coherent after half rotor radius downstream of the propeller. The case $J = 0$ (Fig. 8a) exhibits a clear difference with respect to $J = 0.4$ and a less

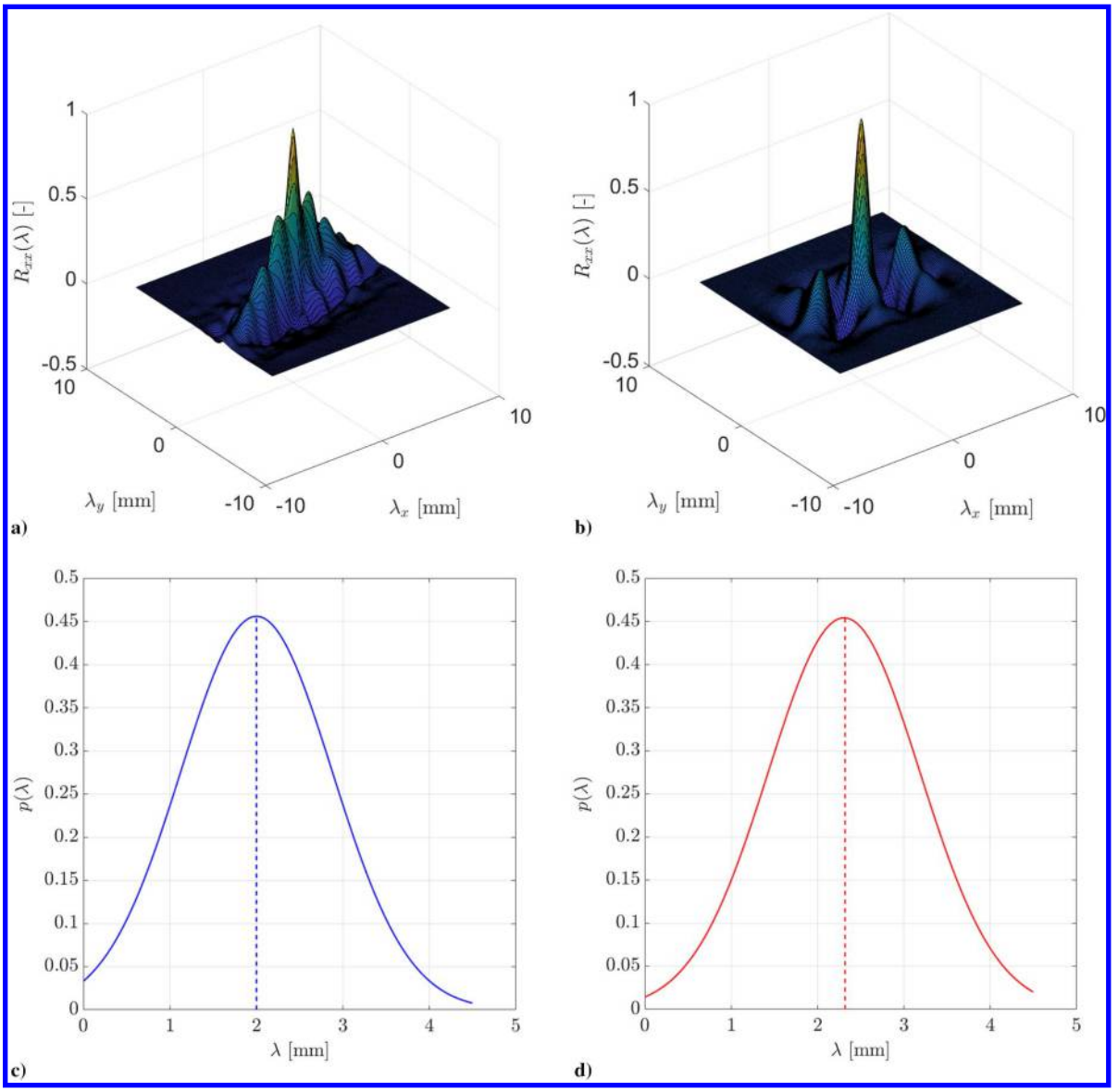

Fig. 7 First row: two-dimensional spatial autocorrelation coefficient of the instantaneous vorticity field in the cross-sectional wake at $J = 0.4$ (a) and $J = 0.6$ (b). Second row: probability density function distribution of the wavelength of the vortices shed from the LSB at $J = 0.4$ (c) and $J = 0.6$ (d).

coherent wake. A spanwise positive/negative vorticity region is barely noticeable, without a visible distribution of vortical structures. Furthermore, this region, together with the tip vortex, appears to dissipate faster and mix with the surrounding flow from about 0.2 rotor radius.

V. Aeroacoustic Characterization

A. Experimental Far-Field Noise Spectra

Figure 9 shows the experimental far-field noise spectra (above $2 \cdot 10^3$ Hz) for the clean blade, computed by using the pressure signals from microphone 2 (mic 2). Spectra from the other microphones show similar trends and do not provide additional information. Figure 9 (left) represents a comparison at a fixed rpm of 4000, by varying the J; Fig. 9 (right) represents instead a comparison at a fixed J of 0.6, by varying the rpm. To highlight the noise trends, a smoothing function that discards the tonal peaks due to the electric motor (as shown by Casalino et al. [22]) is applied to each spectrum and plotted on top of the real spectrum. The hump above $5 \cdot 10^3$ Hz, visible at $J = 0.6$, and to a lesser extent, at $J = 0.4$, is due to the vortex shedding from the LSB. A further indication is given by the Paterson's model [Eq. (5)], which predicts vortex shedding frequencies in the same frequency range. Indeed, since the chord and velocity vary along the blade, there is a range of frequencies (instead of a single tone) at which the vortex shedding noise is expected to be present. For each operating condition, the minimum and maximum vortex shedding frequencies from the last 60% of the blade, predicted by Paterson's law, are reported in Table 3 and contained between $5 \cdot 10^3$ and $4.7 \cdot 10^4$ Hz. The minimum frequencies are also represented in Fig. 9 as vertical lines. For the cross section at the 60% of the span, predictions of the Paterson's frequencies $f_{s_{\text{Pat}}}$ are compared with the experimental shedding frequencies $f_{s_{\text{exp}}}$ calculated in Sec. IV.B. At $J = 0.4$, $f_{s_{\text{Pat}}}$ is equal to 7200 Hz and $f_{s_{\text{exp}}}$ to 9635 Hz with a difference of about 2400 Hz. At $J = 0.6$, $f_{s_{\text{pat}}}$ is 7635 Hz and $f_{s_{\text{exp}}} = 8600$ Hz. These discrepancies are attributed to the simplicity of Paterson's model, which does not take into account the effect of the airfoil profile and to the intrinsic degree of uncertainty of the statistical approach used for the estimation of the shedding frequency.

It is evident that the amplitude of the hump increases when J passes from 0.4 to 0.6. This is associated to the increase in length of the shed vortices (see Sec. IV.B) and, as a consequence, to a more efficient noise source. For the cases $J = 0$ and 0.24, the lower coherence of the vortices at the trailing edge is the reason for the hump reduction. When the rpm is increased and J is kept equal to 0.6 (Fig. 9, right), the hump shifts toward higher frequencies and increases in amplitude. The frequency shifting is in agreement with the Paterson's model as it is dependent on the velocity ($f \propto U^{1.5}$). The increase in amplitude is

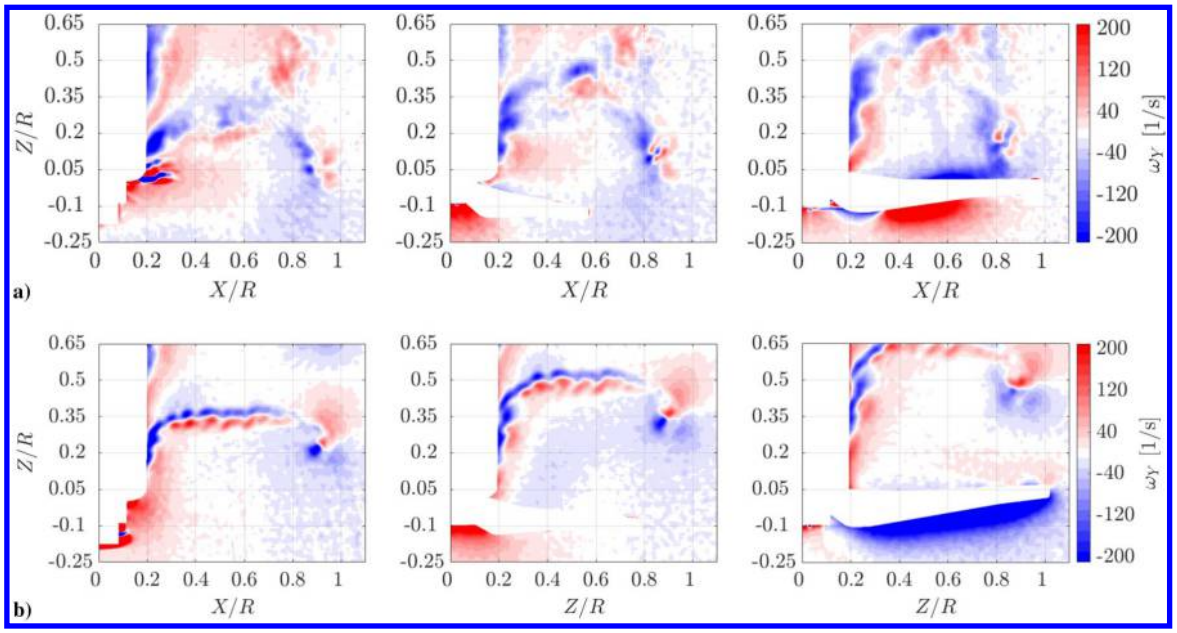

Fig. 8 Instantaneous vorticity distribution in the wake at 4000 rpm and $J = 0$ (a) and $J = 0.4$ (b). The three columns represent three different propeller azimuthal angles: $\psi = 0°$, $\psi = 45°$, and $\psi = 90°$ (from left to right)

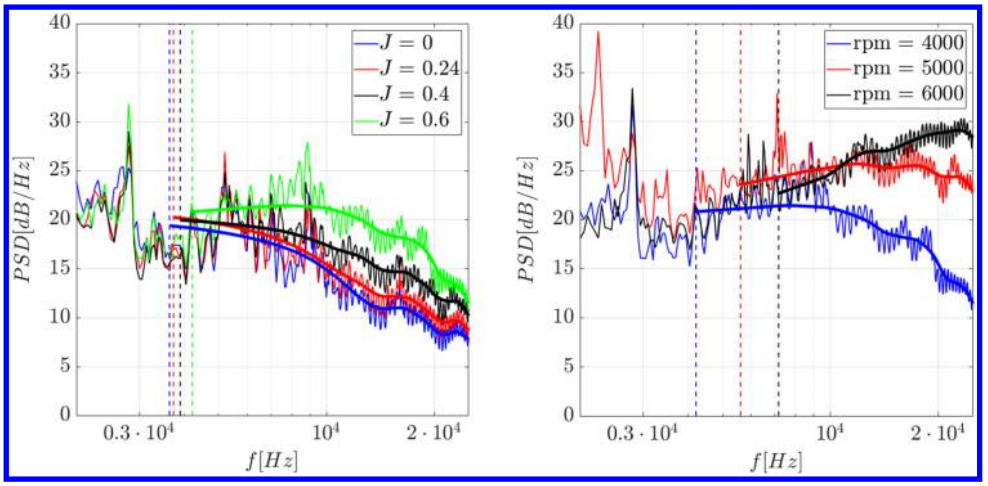

Fig. 9 Comparison of noise spectra at mic 2 for the clean blade at a fixed rpm of 4000, by varying J (left) and a fixed J of 0.6, by varying the rpm (right).

due to the fact that, when the rpm increases (at a fixed J), the angle of attack over the blade decreases, and, as explained above, this shifts the separated area over the trailing edge and make the vortex shedding noise more efficient.

Figure 10 shows the noise spectra for the forced-BL blade. As for the clean case, the left side of each figure reports a comparison at a fixed rpm of 4000, by varying the J, whereas the right side represents a comparison at a fixed J of 0.6, by varying the rpm. The turbulator suppresses the formation of the LSB responsible for the hump. The main noise source for this case is expected to be turbulent boundary-layer trailing edge noise. It is interesting to note that, when the rpm is kept constant and J increases, the hump at $J = 0.4$ and 0.6 disappears and the spectra show the same trend of the cases $J = 0$ and 0.24. This further proves that the high-frequency noise trend for the clean blade is strongly related to the LSB characteristics. On the other side, the increase of rpm at a fixed J of 0.6 causes an increase in the noise level. This could be related to the scaling of trailing edge noise with the Mach number.

Finally, in Figs. 11 and 12 are plotted the results for the forced-BL s.s. and forced-BL p.s. cases, respectively. They confirm that the high-frequency hump is due to an LSB on the suction side of the blade. Indeed, when the turbulator is applied only on the suction side (Fig. 11), the spectra are very similar to the forced-BL case (Fig. 10). When the turbulator is applied only on the pressure side instead (Fig. 12), the hump is still visible and the spectra are similar to the clean case (Fig. 9).

By comparing the noise spectra between the clean, forced-BL, forced-BL s.s., and forced-BL p.s. cases in Fig. 13, the final conclusions about the LSB effect can be more easily inferred. At the lowest advance ratios, i.e., $J = 0$ (Fig. 13a) and 0.24 (Fig. 13b), the LSB, located close to the blade leading edge, has almost no effect and all the spectra have similar levels. At $J = 0.4$ (Fig. 13c) and 0.6 (Fig. 13d), the vortex shedding from the LSB, which

Table 3 Propeller vortex shedding frequencies predicted by means of Paterson's model

	4000 rpm		5000 rpm		6000 rpm	
J	$f_{S_{MIN}}$	$f_{S_{MAX}}$	$f_{S_{MIN}}$	$f_{S_{MAX}}$	$f_{S_{MIN}}$	$f_{S_{MAX}}$
0.00	5,048	25,693	7,055	35,908	9,274	47,202
0.24	5,135	25,806	7,133	36,008	9,345	47,293
0.40	5,288	26,005	7,270	36,187	9,471	47,456
0.60	5,584	26,393	7,537	36,534	9,716	47,774

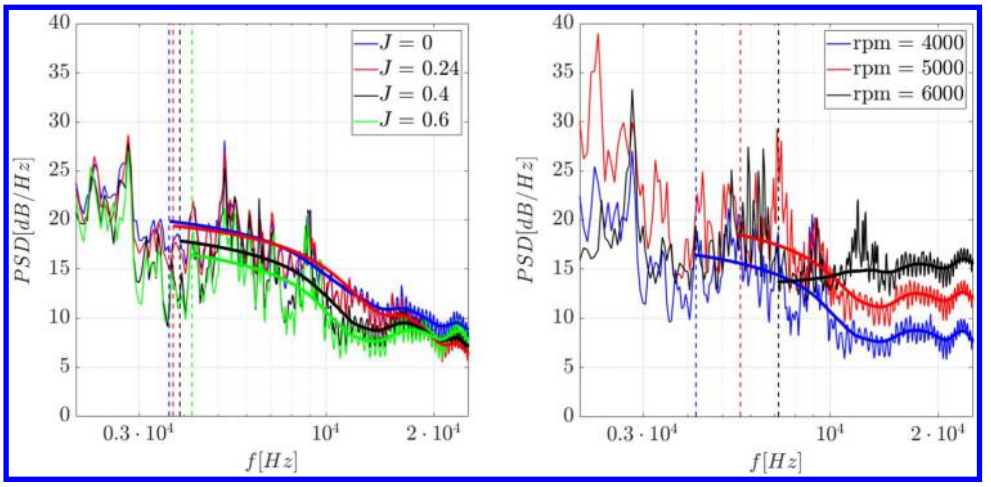

Fig. 10 Comparison of noise spectra at mic 2 for the forced-BL blade at a fixed rpm of 4000, by varying J (left) and a fixed J of 0.6, by varying the rpm (right).

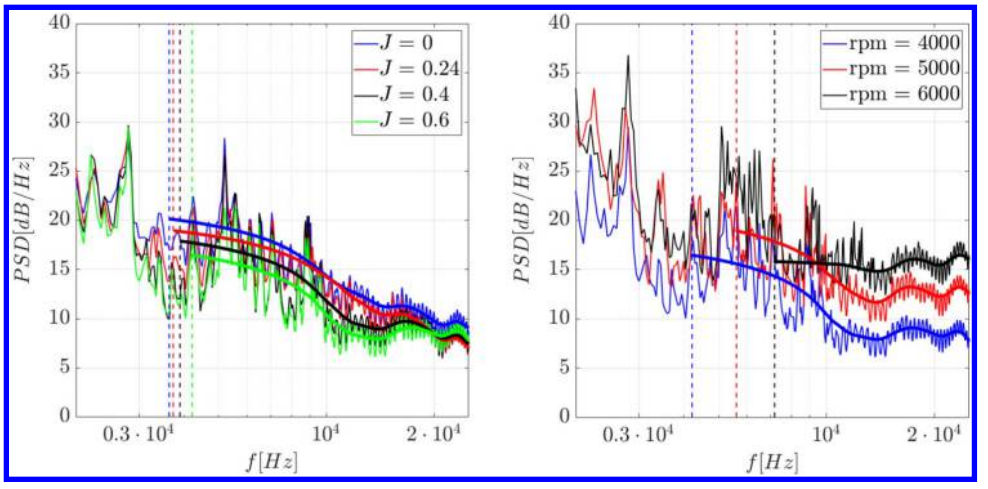

Fig. 11 Comparison of noise spectra at mic 2 for the forced-BL s.s. blade at a fixed rpm of 4000, by varying J (left) and a fixed J of 0.6, by varying the rpm (right).

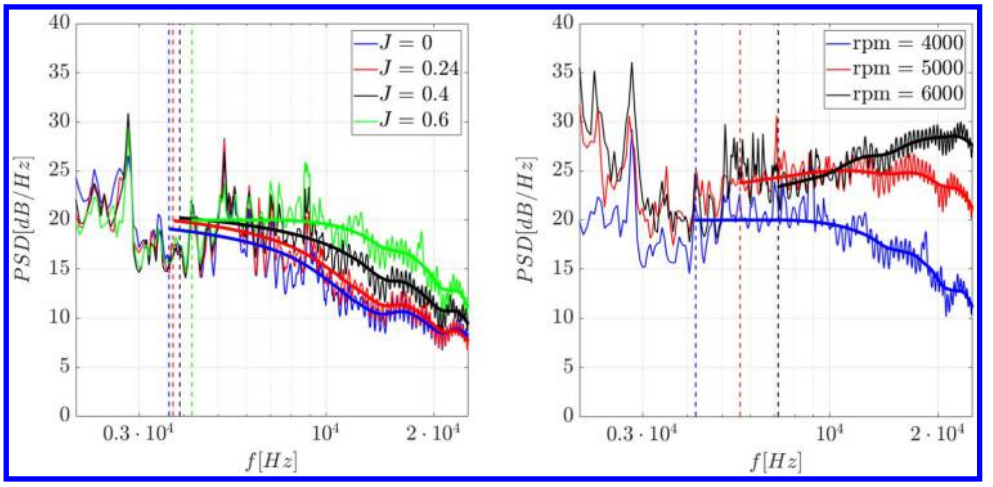

Fig. 12 Comparison of noise spectra at mic 2 for the forced-BL p.s. blade at a fixed rpm of 4000, by varying J (left) and a fixed J of 0.6, by varying the rpm (right).

moves toward the blade trailing edge and increases in chordwise length, is the cause of an increment in noise level for the clean case with respect to the forced-BL and forced-BL s.s. cases of about 5 and 10 dB, respectively. When the turbulator is applied only at the pressure side, as expected, the noise spectra compare well to the clean case. In particular, the level of the forced-BL p.s. spectrum is

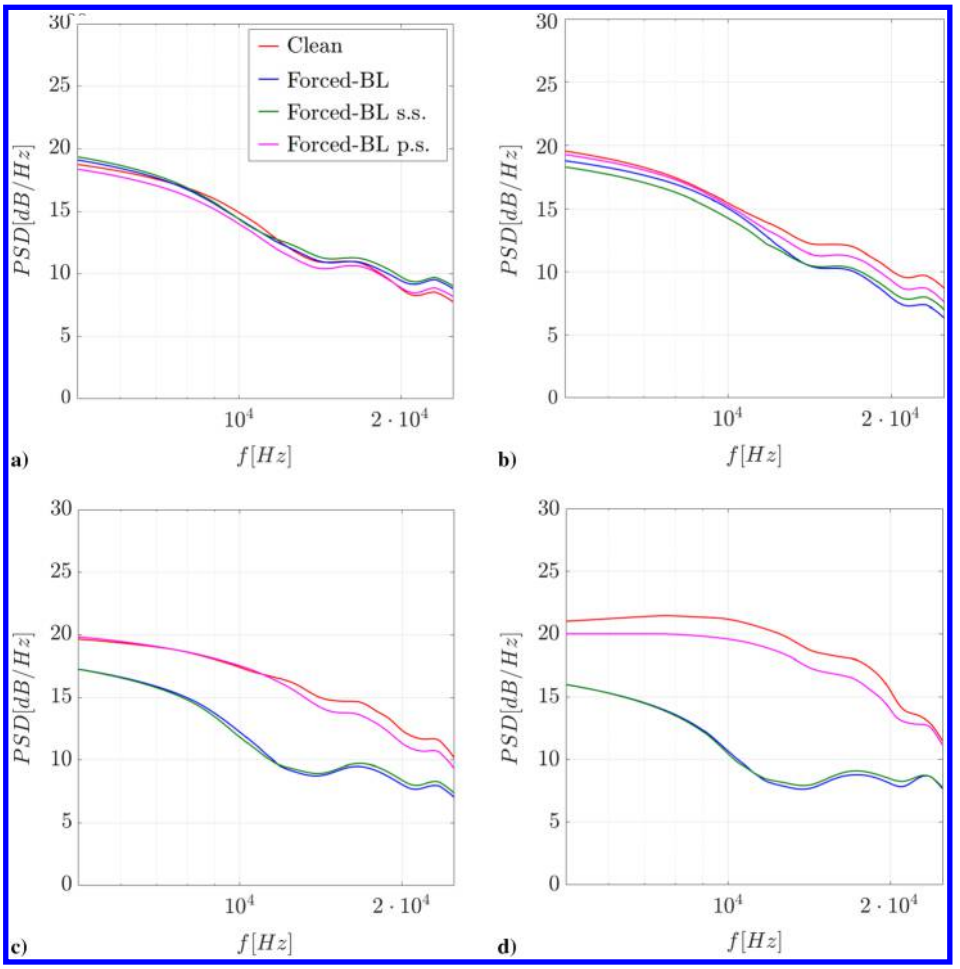

Fig. 13 Comparison at mic 2 between clean, forced-BL, forced-BL s.s., forced-BL p.s. noise spectra at 4000 rpm and $J = 0$ (a), $J = 0.24$ (b), $J = 0.4$ (c), and $J = 0.6$ (d).

about 1 dB (above $1.5 \cdot 10^4$ Hz) and 1.5 dB lower with respect to the clean case at $J = 0.4$ and 0.6, respectively. The slightly lower noise level compared to the clean configuration could be related to a coupling between the events on the two sides of the blade [16]. In other words, the turbulator on the pressure side could influence the position and length of the LSB on the suction side.

B. Noise Prediction from the Semi-Empirical Model

This section presents a discussion about the low-order prediction by means of Eqs. (1) and (2). Figure 14 compares the predictions for the cases $J = 0.4$ and 0.6, which are the ones where the noise due to the shedding from the LSB constitutes the main source, against the experimental noise spectra. The first row illustrates the results at $J = 0.6$ and the second row at $J = 0.4$, whereas the three columns represent the three different rpm, i.e., 4000, 5000, and 6000 (from left to right). At $J = 0.6$, the LSB-VS model predicts sufficiently well the shape and frequency range of the high-frequency hump. The overall mismatch in the amplitude of about 10 dB for all the cases is ascribed to the extreme sensitivity of the BPM model to the angle of attack and not to the present extension for the rotating blade case (see Appendix). If α along the entire blade is varied of about 1 deg for the three cases, the predictions (labeled as "LSB-VS corr.") match the levels of the experimental spectra. It must be noted that the experimental distribution of angles of attack along the blade is not available. Thus, the input angle of attack from Opty∂B-BEMT tool is affected by an uncertainty that is not quantifiable. Only for the case at 5000 rpm, the distribution of α from a high-fidelity simulation, performed by means of Simulia PowerFLOW software based on a lattice Boltzmann/very large eddy method, is also available (see the work from Romani et al. [4] for the details). The result using this α distribution is included in Fig 14b (denoted as LBL-VS PF) and it compares well with the "corrected" result using α from Opty∂B-BEMT. At $J = 0.4$, the amplitude of the numerical predictions from the LSB-VS model compares well to the experiments after the angle-of-attack "correction." On the other hand, the predicted frequency range is narrower with respect to the experimental values, which exhibit a broaden hump. At both the advance ratios, the TBL-TE model provides significantly lower levels, hence excluding trailing edge noise as one of the major noise sources. Furthermore, in this case a correction of the input α would not improve the match with the experimental values because the TBL-TE model is much less sensitive to a variation of α, as shown in the Appendix.

Figure 15a represents the noise spectrum in 1/3-octave (thick black line) at microphone 2 for the case at $J = 0.6$ and 4000 rpm, together with the contribution from each individual blade strip, where the blue lines represent the contribution of the sections up to $r/R = 0.7$ and the red lines from $r/R = 0.7$ onward. It is conjectured that the broad hump is due to the superimposition of tones of different amplitudes and frequencies, emitted from the single blade sections. Furthermore, the last 30% of the blade (red lines) has the largest contribution in terms of noise generation, and it is responsible for most of the hump. Due to the lower relative velocity and higher angle of attack, the more inboard sections (blue lines) generate tones of much lower amplitude. This can be better visualized by plotting the azimuthal overall sound pressure level (OASPL) contribution in the propeller plane, as in Fig. 15b. The right outboard part of the disc shows an higher noise level (between 2 and 4 dB) with respect to the corresponding parts on the other sides and makes the plot asymmetric. This is due to the Doppler effect. The other cases present similar results, and hence they are not reported.

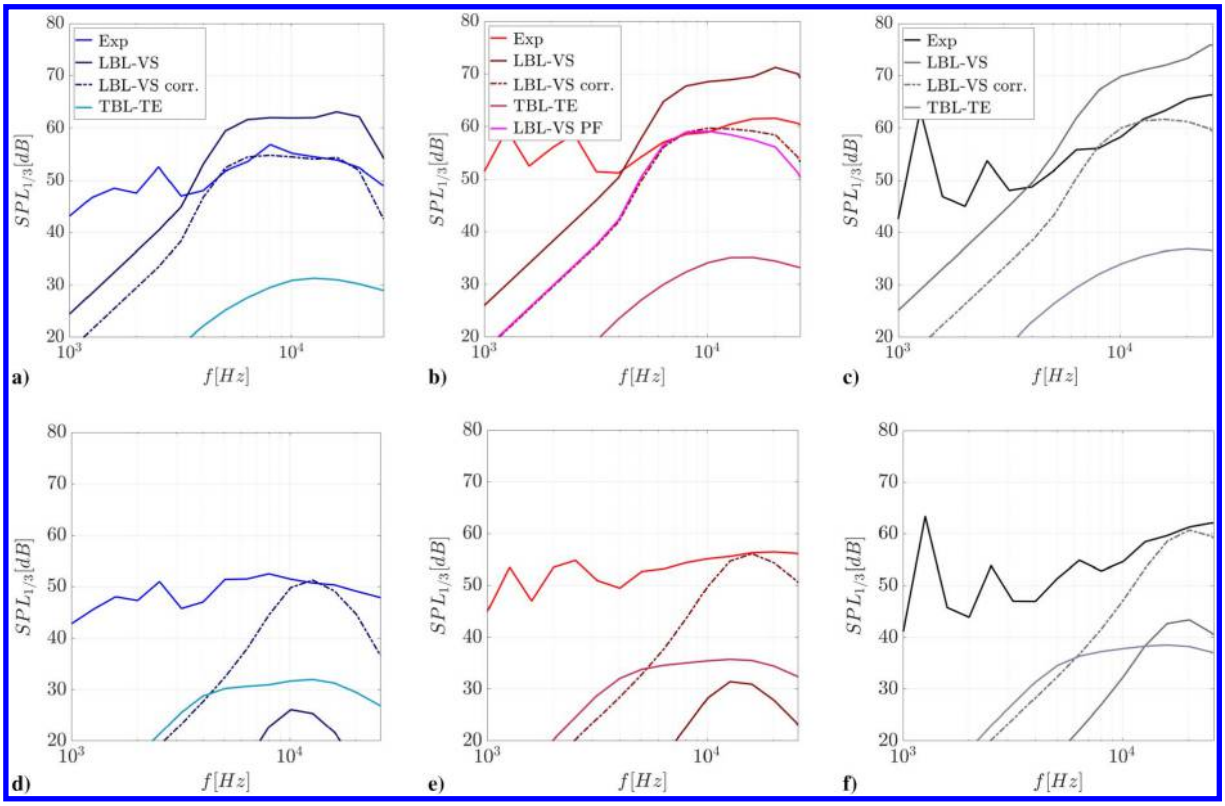

Fig. 14 Comparison at mic 2 between the experimental noise spectra and the numerical predictions at $J = 0.6$ and 4000 rpm (a), $J = 0.6$ and 5000 rpm (b), $J = 0.6$ and 6000 rpm (c), $J = 0.4$ and 4000 rpm (d), $J = 0.4$ and 5000 rpm (e), and $J = 0.4$ and 6000 rpm (f).

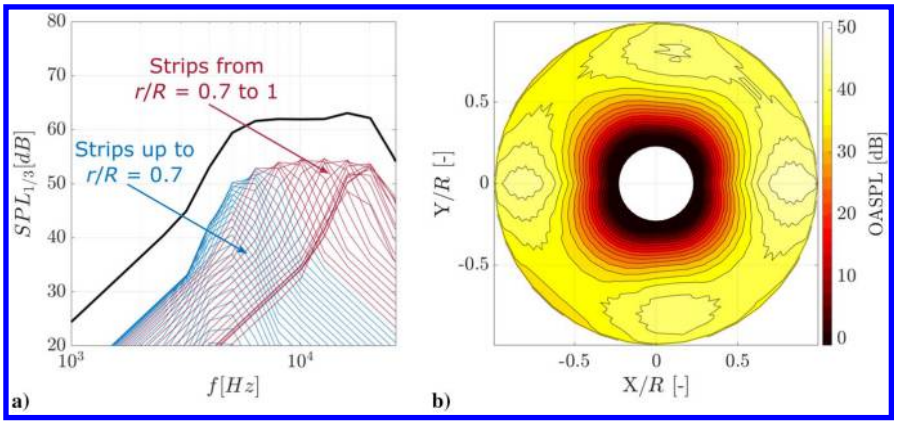

Fig. 15 Sectional contribution to the numerical noise spectrum (a) and azimuthal OASPL contribution (b) at mic 2 for $J = 0.6$ and 4000 rpm.

VI. Conclusions

An investigation of the noise emitted by an LSB on a small-scale propeller operating at low Reynolds number was accomplished through experimental measurements in an anechoic wind tunnel. The propeller was tested both with a smooth surface (clean) and with a turbulator applied on the suction side of the propeller blades (forced-BL s.s.), on the pressure side (forced-BL p.s.), and on both suction and pressure sides (forced-BL) to force the transition of the boundary layer from laminar to turbulent. Microphone measurements were complemented with oil-flow visualization of the blade surface and phase-locked PIV measurements of a blade cross section and of the propeller slipstream. Physical insights of noise generation due to the LSB were retrieved by extending the semi-empirical BPM model [17] to rotating blades.

An LSB was visualized on the suction side of the clean blade surface at $J = 0$, 0.24, and 0.4. At $J = 0.6$ the LSB probably bursts because there was not a visual evidence of flow reattachment. When the boundary-layer transition location is forced, the LSB was suppressed and the flow appeared to be attached after the transition strip. The analysis of the instantaneous vorticity field around the cross section at the 60% of the span revealed that the LSB is responsible for vortex shedding, characterized by coherent structures in the wake for the cases $J = 0.4$ and 0.6. The bigger length scale of the shed vortices at $J = 0.6$ was associated with the hypothesis of separation without reattachment. The shedding frequency, calculated by means of a statistical approach, was found to be 9635 and 8600 Hz at $J = 0.4$ and 0.6, respectively. Vortical coherent structures were not clearly visible for the cases $J = 0$ and 0.24, and this was attributed to the loss of coherence due to the smaller chordwise length of the LSB and the closer vicinity of the latter to the blade leading edge.

The vortex shedding from the LSB at the suction side of the propeller blades is responsible for a high-frequency hump in the far-field noise spectra at $J = 0.4$ and 0.6. In accordance with the Paterson's model, the hump shifts toward higher frequencies when the rpm is increased. The comparison between clean and forced-BL noise spectra showed that, when the turbulator is used on both pressure and suction sides or only at the suction side, the hump was removed and the noise was reduced of about 5 dB at $J = 0.4$

and 10 dB at $J = 0.6$. This constitutes a further prove of the link between the LSB and high-frequency noise radiation.

The application of the semi-empirical model revealed that the different spanwise blade sections emit tones at different amplitudes and frequencies, because of the variation of the relative velocity and angle of attack along the blade. Hence, the hump in the noise spectra is due to the superposition of the same tones. The comparison of the numerical predictions against the experimental results showed that the model satisfactory predicts the frequency range of the hump. The mismatch found for the amplitude was proven to be associated to an extreme sensitivity of the BPM model itself to the angle of attack. A variation of angle of attack over the entire blade of about 1 deg let the numerical predictions to match well with the experiments.

Appendix: Sensitivity of BPM Model to α

In this section the sensitivity of the LBL-VS and TBL-TE noise models to the angle of attack α is evaluated. To this purpose, a fixed wing with a NACA 4412 airfoil (the same adopted for the propeller blades of the present study) is considered and α is varied from 0 to 6 deg. The wing has a chord length of 0.03 m/s, a span of 0.15 m, and it is operated at a freestream velocity of 50 m/s, corresponding to a chord Reynolds number of 10^5. The noise is evaluated at a distance of 3 m from the midspan of the wing. The results for the two noise models are plotted in Figs. A1 and A2, where the left side shows the output noise spectra for each α, whereas the right side represents the ΔSPL, which is the difference in the noise level when a variation of 1 deg of angle of attack is applied. For each α, the difference is calculated with respect to the previous one.

For the LSB-VS noise model, when α is increased, the level of the predicted tone reduces substantially. Furthermore, a change of α has only an effect on the amplitude of the tone and not on the frequency. It appears that only when α is varied from 0 to 1 deg the ΔSPL is below 10 dB, whereas for all the other cases a variation higher than 10 dB is found. The maximum variation found is 19 dB and corresponds to a change of α from 2 to 3 deg. This high sensitivity of the model to a change of angle of attack might be not very realistic and should be verified against experimental data.

On the other side, the TBL-TE noise model shows an increase in the noise level and a shift toward lower frequencies when α is increased. In this case, the model is much less sensitivity to the angle of attack. Indeed, the ΔSPL found varies from 1 dB up to a maximum of 2 dB.

References

[1] Winslow, J., Otsuka, H., Govindarajan, B., and Chopra, I., "Basic Understanding of Airfoil Characteristics at Low Reynolds Numbers (104–105)," *Journal of Aircraft*, Vol. 55, No. 3, 2017, pp. 1–12. https://doi.org/10.2514/1.C034415

[2] Grande, E., Romani, G., Ragni, D., Avallone, F., and Casalino, D., "Aeroacoustic Investigation of a Propeller Operating at Low Reynolds Numbers," *AIAA Journal*, Vol. 60, No. 2, 2021, pp. 1–12. https://doi.org/10.2514/1.J060611

[3] Leslie, A., Wong, K. C., and Auld, D., "Experimental Analysis of the Radiated Noise from a Small Propeller," *Proceedings of 20th International Congress on Acoustics, ICA*, 2010.

[4] Romani, G., Grande, E., Avallone, F., Ragni, D., and Casalino, D., "Performance and Noise Prediction of Low-Reynolds Number Propellers

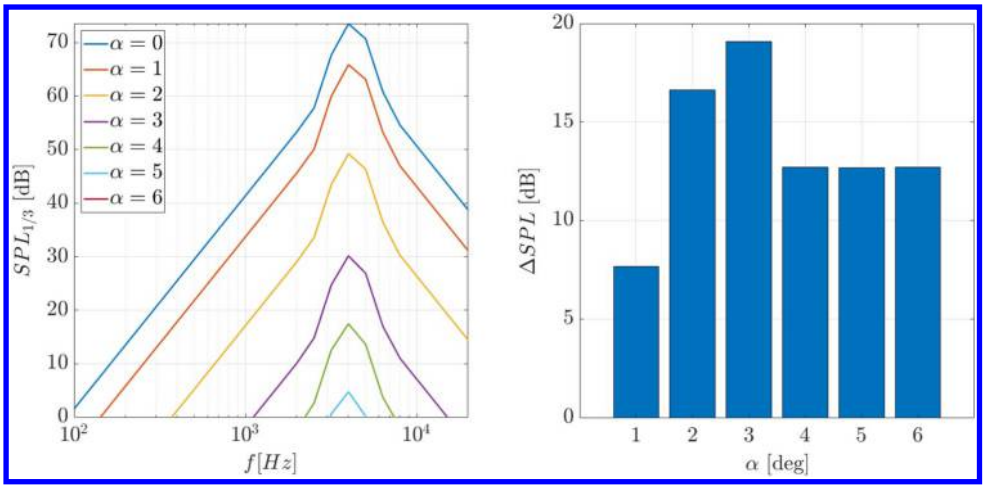

Fig. A1 LBL-VS noise model results for a straight wing at different α (left). Variation of the noise level ΔSPL with respect to a change of α of 1 deg (right).

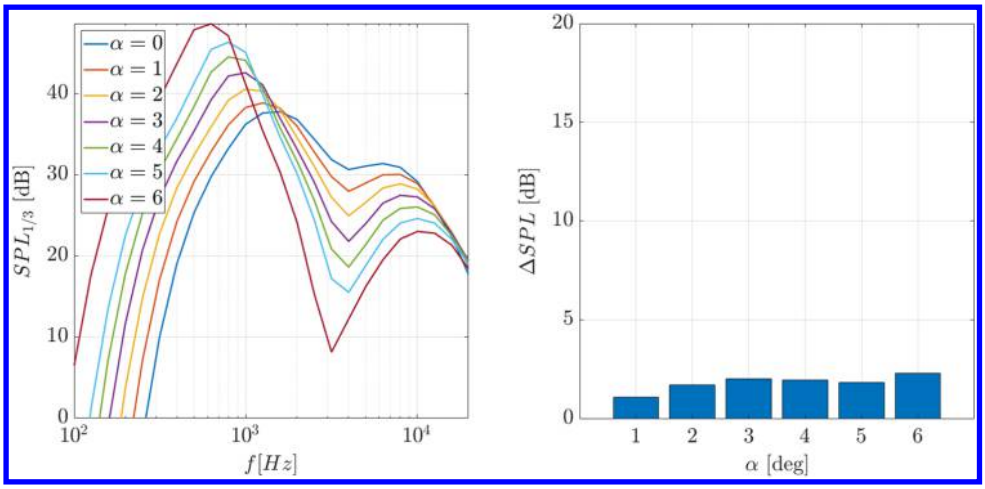

Fig. A2 TBL-TE noise model results for a straight wing at different α (left). Variation of the noise level ΔSPL with respect to a change of α of 1 deg (right).

Using the Lattice-Boltzmann Method," *Aerospace Science and Technology*, Vol. 125, June 2021, Paper 107086.
https://doi.org/10.1016/j.ast.2021.107086

[5] Huff, D. L., and Henderson, B. S., "Electric Motor Noise for Small Quadcopters: Part 1—Acoustic Measurements," *2018 AIAA/CEAS Aeroacoustics Conference*, AIAA Paper 2018-2952, 2018.
https://doi.org/10.2514/6.2018-2952

[6] Henderson, B. S., and Huff, D., "Electric Motor Noise for Small Quadcopters: Part II—Source Characteristics and Predictions," *2018 AIAA/CEAS Aeroacoustics Conference*, AIAA Paper 2018-2953, 2018.
https://doi.org/10.2514/6.2018-2953

[7] Boutilier, M., and Yarusevych, S., "Parametric Study of Separation and Transition Characteristics over an Airfoil at Low Reynolds Numbers," *Experiments in Fluids*, Vol. 52, 2012, pp. 1491–1506.
https://doi.org/10.1007/s00348-012-1270-z

[8] Yarusevych, S., Sullivan, P., and Kawall, J., "Coherent Structures in an Airfoil Boundary Layer and Wake at Low Reynolds Numbers," *Physics of Fluids*, Vol. 18, 2006, Paper 044101.
https://doi.org/10.1063/1.2187069

[9] Marchman, J. F., and Abtahi, A., "Aerodynamics of an Aspect Ratio 8 Wing at Low Reynolds Numbers," *Journal of Aircraft*, Vol. 22, No. 7, 1985, pp. 628–634.
https://doi.org/10.2514/3.45176

[10] Park, D., Shim, H., and Lee, Y., "PIV Measurement of Separation Bubble on an Airfoil at Low Reynolds Numbers," Vol. 33, No. 1, 2020, Paper 04019105.
https://doi.org/10.2514/6.2020-3644

[11] Pröbsting, S., and Yarusevych, S., "Laminar Separation Bubble Development on an Airfoil Emitting Tonal Noise," *Journal of Fluid Mechanics*, Vol. 780, Sept. 2015, pp. 167–191.
https://doi.org/10.1017/jfm.2015.427

[12] Arcondoulis, E., Doolan, C., Zander, A., and Brooks, L., "A Review of Trailing Edge Noise Generated by Airfoils at Low to Moderate Reynolds Number," *Acoustics Australia/Australian Acoustical Society*, Vol. 36, No. 3, 2011, p. 135.

[13] Arbey, H., and Bataille, J., "Noise Generated by Airfoil Profiles Placed in a Uniform Laminar Flow," *Journal of Fluid Mechanics*, Vol. 134, Sept. 1983, pp. 33–47.
https://doi.org/10.1017/S0022112083003201

[14] Paterson, R. W., Vogt, P. G., Fink, M. R., and Munch, C. L., "Vortex Noise of Isolated Airfoils," *Journal of Aircraft*, Vol. 10, No. 5, 1973, pp. 296–302.
https://doi.org/10.2514/3.60229

[15] Nash, E. C., Lowson, M. V., and McAlpine, A., "Boundary-Layer Instability Noise on Aerofoils," *Journal of Fluid Mechanics*, Vol. 382, March 1999, pp. 27–61.
https://doi.org/10.1017/S002211209800367X

[16] Pröbsting, S., Scarano, F., and Morris, S., "Regimes of Tonal Noise on an Airfoil at Moderate Reynolds Number," *Journal of Fluid Mechanics*, Vol. 780, Oct. 2015, pp. 407–438.
https://doi.org/10.1017/jfm.2015.475

[17] Brooks, T., Pope, D., and Marcolini, M., "Airfoil Self-Noise and Prediction," NASA Reference Publication 1218, NASA, 1989.

[18] Merino-Martinez, R., Rubio Carpio, A., Lima Pereira, L., Herk, S., Avallone, F., Ragni, D., and Kotsonis, M., "Aeroacoustic Design and Characterization of the 3D-Printed, Open-Jet, Anechoic Wind Tunnel of Delft University of Technology," *Applied Acoustics*, Vol. 170, Dec. 2020, Paper 107504.
https://doi.org/10.1016/j.apacoust.2020.107504

[19] Scarano, F., and Riethmuller, M., "Advances in Iterative Multigrid PIV Image Processing," *Experiments in Fluids*, Vol. 29, No. 1, 2000, pp. S051–S060.
https://doi.org/10.1007/s003480070007

[20] Willert, C., "Stereoscopic Digital Particle Image Velocimetry for Application in Wind Tunnel Flows," *Measurement Science and Technology*, Vol. 8, No. 12, 1997, p. 1465.
https://doi.org/10.1088/0957-0233/8/12/010

[21] Westerweel, J., "Fundamentals of Digital Particle Image Velocimetry," *Measurement Science and Technology*, Vol. 8, No. 12, 1997, p. 1379.
https://doi.org/10.1088/0957-0233/8/12/002

[22] Casalino, D., Grande, E., Romani, G., Ragni, D., and Avallone, F., "Definition of a Benchmark for Low Reynolds Number Propeller Aeroacoustics," *Aeroaspace Science and Technology*, Vol. 113, 2021, Paper 106707.

[23] Antonio, P., Barbarino, M., Casalino, D., and Federico, L., "Tonal and Broadband Noise Calculations for Aeroacoustic Optimization of a Pusher Propeller," *Journal of Aircraft*, Vol. 47, No. 3, 2010, pp. 835–848.
https://doi.org/10.2514/1.45315

[24] Anderson, J. D., *Fundamentals of Aerodynamics*, 4th ed., McGraw–Hill, New York, 2007, Chap. 18.

[25] Toppings, C. E., and Yarusevych, S., "Structure and Dynamics of a Laminar Separation Bubble Near a Wingtip," *Journal of Fluid Mechanics*, Vol. 929, Dec. 2021, p. A39.
https://doi.org/10.1017/jfm.2021.881

[26] Bastedo, W. G., Jr., and Mueller, T. J., "Spanwise Variation of Laminar Separation Bubbles on Wings at Low Reynolds Number," *Journal of Aircraft*, Vol. 23, No. 9, 1986, pp. 687–694.
https://doi.org/10.2514/3.45363

[27] Yarusevych, S., Sullivan, P., and Kawall, J., "On Vortex Shedding from an Airfoil in Low-Reynolds-Number Flows," *Journal of Fluid Mechanics*, Vol. 632, Aug. 2010, p. 245.
https://doi.org/10.1017/S0022112009007058

X. Zhang
Associate Editor